Illuminating Molecular Symmetries with Bicircular High-Order-Harmonic Generation

Daniel M. Reich and Lars Bojer Madsen
Department of Physics and Astronomy, Aarhus University, DK-8000 Aarhus C, Denmark
(Received 1 July 2016; published 22 September 2016)

We present a general theory of bicircular high-order-harmonic generation from N-fold rotationally symmetric molecules. Using a rotating frame of reference we predict the complete structure of the high-order-harmonic spectra for arbitrary driving frequency ratios and show how molecular symmetries can be directly identified from the harmonic signal. Our findings reveal that a characteristic fingerprint of rotational molecular symmetries can be universally observed in the ultrafast response of molecules to strong bicircular fields.

DOI: 10.1103/PhysRevLett.117.133902

High-order-harmonic generation (HHG) represents one of the primary gateways towards obtaining novel tabletop light sources with unique properties for a wide range of applications [1]. At the same time it holds the promise to revolutionize our understanding of fundamental dynamical processes in atoms and molecules, demonstrated, for example, by the ultrafast tracing of charge dynamics [2,3], as well as in condensed-matter systems, exemplified by the advent of extreme ultraviolet spectroscopy in solids [4]. While the generation of bright linearly polarized light through HHG is well established [5], efforts to expand the toolbox of ultrafast light probes towards circular and elliptical polarization have subsequently attracted great interest, motivated by the vast potential for applications in, e.g., the study of circular dichroism in chiral molecules [6] or the measurement of quantum phases [7,8]. The most promising approach, namely, the HHG of circularly polarized light by bicircular driving, has recently garnered much attention due to several groundbreaking experiments demonstrating tunable polarization through helicity-selective phase matching [9–11], the generation of isolated attosecond pulses [12], the extension into the x-ray regime [13], and even detailed three-dimensional tomography of the HHG fields [14]. Even though the generation of circularly polarized pulses via HHG was examined already in the 1990s [15–20] these experimental studies reinvigorated interest also from the theoretical side particularly regarding the question of selection rules [21,22] and the role of molecular and orbital symmetries [23,24]. Most notably, a recent article provided a detailed analysis on the correlation between symmetries and HHG spectra in both atoms and molecules [25]. However, these studies mostly focused on the simplest bicircular HHG scheme, which involves a circularly polarized driver with a fundamental frequency ω and another driver with opposite circular polarization at 2ω. For atomic targets one observes in this setup harmonics of opposite circular polarization at frequencies $(3n+1)\omega$ and $(3n+2)\omega$ $(n \in \mathbb{N})$ whereas no signal is observed for frequencies $3n\omega$. For molecular targets this pattern generally becomes more elaborate [24,25].

In a previous work [26] we argued that bicircular HHG can be understood in a rotating frame of reference. For axially symmetric targets the neighboring HHG peaks in the laboratory frame can be regarded as originating from a linearly polarized harmonic in the rotating frame. This explains, e.g., the similar emission strength of those two harmonics from s states in atomic targets [25]. While the orbital symmetry influences the relative strength, the molecular symmetry can lead to the appearance and complete disappearance of certain peaks in the spectrum. Although the connection between dynamical symmetries and HHG selection rules has been known for a long time [27–29], the impact of the molecular symmetry for bicircular driving was discussed only recently [24,25]. Still, the focus was mostly on specific driving-field configurations under particular rotational symmetries. Here, using the rotating-frame picture, we show that the fingerprint of arbitrary N-fold rotational molecular symmetries can be found in any bicircular driving scheme with pulses of equal strength pointing towards the possibility of the ultrafast readout of molecular symmetries in, e.g., chemical reactions.

We briefly review the rotating-frame transformation for a field-free Hamiltonian H_0 under the influence of the electric field of two counterrotating circularly polarized pulses with envelope $F_0(t)$ and frequencies ω, ω' polarized in the xy plane

$$H(t) = H_0 + F_0(t)[x\cos(\omega t) + y\sin(\omega t) + x\cos(\omega' t) - y\sin(\omega' t)]. \quad (1)$$

Although we employ a single-active-electron picture it is straightforward to show that the discussion holds when multiple electrons are considered, see the Supplemental Material [30].

The unitary transformation $U(t) = e^{-i\alpha t L_z}$ with $\alpha = (\omega' - \omega)/2$ and L_z the angular momentum operator describing rotation around the z axis leads to the Hamiltonian in the rotating frame

$$H'(t) = H_0'(t) + \alpha L_z + 2F_0(t)x\cos(\tilde{\omega}t), \quad (2)$$

where $\tilde{\omega} = (\omega + \omega')/2$ and $H_0'(t) = U(t)H_0U^\dagger(t)$ [26]. The right-circularly polarized (RCP) [left-circularly polarized (LCP)] signal in the laboratory frame $S^{\text{lab}}(\Omega)$ is obtained via the corresponding signal in the rotating frame shifted in frequency by α to the left [to the right] [26]

$$S^{\text{lab}}_{\text{RCP}}(\Omega - \alpha) = S^{\text{rot}}_{\text{RCP}}(\Omega), \qquad S^{\text{lab}}_{\text{LCP}}(\Omega + \alpha) = S^{\text{rot}}_{\text{LCP}}(\Omega). \tag{3}$$

These formulas are valid even in the absence of axial symmetry. In a nonaxially symmetric setting, however, the linearly polarized driver in the rotating frame now irradiates a rotating target. As such, the simple selection rule leading to only odd multiples of the driving frequency in the rotating frame ceases to be valid.

Since the bicircular driving field is polarized in the xy plane the HHG process is well described in two dimensions. We can simplify our discussion even further by focusing on the projection of the molecular potential in the x direction in the rotating frame, i.e., $V(x,t) \equiv V(x, y = 0, t)$. This is motivated by the fact that the driving field in the rotating frame is linearly polarized in the x direction and the ground-state wave function is centered at the rotational center, i.e., $\langle y \rangle = 0$. Thus, ionization events, which are the first step in HHG [31–33], are centered around $y = 0$. Moreover, the deflection from the angular momentum term in the rotating frame, usually called the Coriolis term, is generally negligible even for moderately high values of α [26]. In particular, it alters neither the inversion symmetry nor the selection rules.

The molecular potential in the rotating frame inherits a dynamical symmetry if a static N-fold rotational symmetry in the laboratory frame is present in the polarization plane of the bicircular driver,

$$V(x,t) = V\left(x, t + \frac{2\pi}{N\alpha}\right). \tag{4}$$

We choose $t = 0$ such that $V(x,t) = V(x,-t)$, i.e., at time zero the potential is symmetric with respect to reflection on the x axis, cf. Fig. 1. This allows us to express the potential in a Fourier series as follows:

$$V(x,t) = V_0(x) + \sum_{k\neq 0} V_k(x)\cos(Nk\alpha t), \tag{5}$$

where

$$V_k(x) = \frac{N\alpha}{2\pi}\int_0^{(2\pi/N\alpha)} V(x,t)\cos(Nk\alpha t)dt.$$

At this point it becomes important to distinguish between even and odd N. For even N one observes that $V(x,t) = V(-x,t) \quad \forall\ t$; hence, all $V_k(x)$ are even, too. For odd N one obtains instead $V(x,t) = V\big(-x, t + (2\pi/2N\alpha)\big)$ since after half a period the potential inverts in the x direction, cf. Fig. 1, and inserting this relation in Eq. (5) leads to

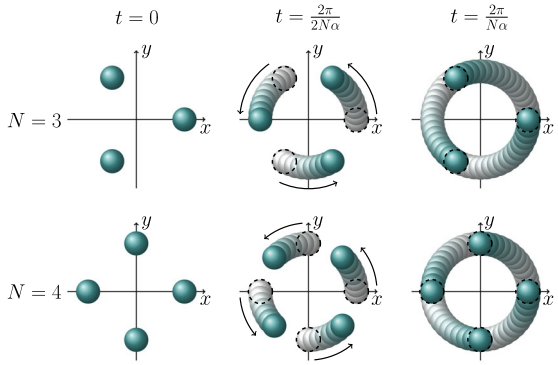

FIG. 1. Illustration of nuclear rotation in the rotating frame for N-fold rotational symmetry with $N = 3, 4$. The position of the nuclei recurs after a period of $2\pi/(N\alpha)$; the initial position is indicated for reference by a dashed circle. At the half point $t = 2\pi/(2N\alpha)$ the projected potential in the x direction inverts for odd N whereas for even N the inversion symmetry is preserved for all times.

$$V_0(x) + \sum_{k\neq 0} V_k(x)\cos(Nk\alpha t) = V_0(-x) + \sum_{k\neq 0}(-1)^k V_k(-x)\cos(Nk\alpha t).$$

Evidently, $V_k(x)$ is even for even k (including $k = 0$) whereas it is odd for odd k. The Hamiltonian in the rotating frame thus reads

$$H'(t) = T + V_0(x) + \alpha L_z + 2F_0(t)x\cos(\tilde{\omega}t) + \sum_{k\neq 0} V_k(x)\cos(Nk\alpha t) \tag{6}$$

with T the kinetic energy operator and $V_0(x)$ the even time-averaged part of the potential. The form of Eq. (6) allows us to interpret the time dependence of the molecular potential in the rotating frame as additional driving fields with frequencies $Nk\alpha$ that couple spatially via the coefficient $V_k(x)$. We call these fields "virtual" driving fields, as opposed to the "actual" driving. They appear due to the transformation to the rotating frame and the resulting rotation of the nuclei therein. The virtual driving has a perturbative character since its strength is related to the strength of the Coulomb potential. Specifically, when the electron gathers energy in the continuum, particularly for higher harmonics with corresponding long excursions from the ionic core, the effect of the virtual driving is decreased with distance.

The interplay between actual and virtual driving gives rise to a set of characteristic line features in the HHG spectra if one varies over different values of α for fixed $\tilde{\omega}$. Harmonic emission is associated with the dipolar response by the driven system. In all cases $V_0(x)$ is even such that the combined parity of actual and virtual driving needs to be odd to obtain a dipolar radiation signal, cf. Table I. In a photon picture, for even N this is only possible if an odd number of photons is absorbed by the actual driver since the virtual driving is always even. No participation ($k = 0$) of

TABLE I. Possible combinations of actual and virtual driving (as defined in the main text) with the corresponding parity indicated by [+] (even) and [−] (odd). The total parity is the product of the constituents' parities. Signals with even total parity are forbidden (indicated by ⊗). Signals with high order $|k|$ in the virtual driving, cf. Eq. (6), are generally expected to be less pronounced.

	V_0	Actual driver	Virtual driver	Total	Line
N odd	[+]	$m\tilde{\omega}$, m odd [−]	None [+]	[−]	Main
	[+]	$m\tilde{\omega}$, m odd [−]	$\pm N\alpha$[−]	[+]	⊗
	[+]	$m\tilde{\omega}$, m odd [−]	$\pm 2N\alpha$[+]	[−]	2nd side
	[+]	$\bar{m}\,\tilde{\omega}$, $\bar{m}$ even [+]	None [+]	[+]	⊗
	[+]	$\bar{m}\,\tilde{\omega}$, $\bar{m}$ even [+]	$\pm N\alpha$[−]	[−]	1st side
	[+]	$\bar{m}\,\tilde{\omega}$, $\bar{m}$ even [+]	$\pm 2N\alpha$[+]	[+]	⊗
N even	[+]	$m\tilde{\omega}$, m odd [−]	None [+]	[−]	Main
	[+]	$m\tilde{\omega}$, m odd [−]	$\pm N\alpha$[+]	[−]	1st side
	[+]	$m\tilde{\omega}$, m odd [−]	$\pm 2N\alpha$[+]	[−]	2nd side
	[+]	$\bar{m}\,\tilde{\omega}$, $\bar{m}$ even [+]	None [+]	[+]	⊗
	[+]	$\bar{m}\,\tilde{\omega}$, $\bar{m}$ even [+]	$\pm N\alpha$[+]	[+]	⊗
	[+]	$\bar{m}\,\tilde{\omega}$, $\bar{m}$ even [+]	$\pm 2N\alpha$[+]	[+]	⊗

the virtual driver leads to a signal at frequencies $m\tilde{\omega}$ for odd m (the main line) as well as additional signatures at $m\tilde{\omega} \pm N|k|\alpha$ for odd m and arbitrary $|k| > 0$ (the side lines). For odd N there are two possibilities. If an odd number of photons is absorbed from the actual driver then the virtual driver needs to make an even contribution. This includes no contribution, creating the main line at $m\tilde{\omega}$, and the leading-order even contribution $\pm 2N\alpha$, giving rise to secondary side lines ($|k| = 2$) at $m\tilde{\omega} \pm 2N\alpha$ for odd m. However, the primary side lines ($|k| = 1$) can be found at $\bar{m}\,\tilde{\omega} \pm N\alpha$ for even $\bar{m}$ combining an even number of photons absorbed from the actual driver with the leading odd virtual driving contribution at $\pm N\alpha$.

Because of the comparatively small impact of the Coriolis term the emitted harmonics in the rotating frame are approximately linearly polarized [26]. Thus, by Eqs. (3), they contribute roughly equally to the RCP and LCP signals in the laboratory frame. The positions of the main as well as the first two side lines in the general case are shown at the top of Table II.

It is instructive to discuss a particular example following from these general predictions. To this end we consider a threefold molecular symmetry under the driving-field configurations $\omega' = 2\omega$ and $\omega' = 3\omega$ in Eq. (1). The lower part of Table II summarizes the expected main and side lines in these two settings according to our model, expressed in terms of multiples of ω. The polarization of particular peaks in the HHG spectrum is determined by the superposition of the contributions from the main and side lines. For $\omega' = 2\omega$ all main and side lines with a given circular polarization coincide leading to alternating right- and left-circular polarization [RCP at $(3n+1)\omega$ and LCP at $(3n+2)\omega$, $n \in \mathbb{N}$]. Conversely, for $\omega' = 3\omega$ there exist secondary side-line contributions with opposite polarization compared to the main lines at $(4n+1)\omega$ and $(4n+3)\omega$. Furthermore, there is both a left- and right-circular contribution at the level of a primary side line at $4n\omega$ and $(4n+2)\omega$. In the former case we expect the total signal to be predominantly circularly polarized since the secondary side lines are expected to be much weaker than the main line. For the latter case the superposition occurs for side lines of the same order; hence, we expect the result to be close to linearly polarized. These predictions are in perfect agreement with the theoretical analysis and numerics shown in Ref. [24]. We note, however, that in some settings superpositions between, e.g., main and primary side lines, may occur and a precise prediction on the resulting polarization of the total signal would require a more in-depth analysis.

To illustrate our model's high degree of predictability we performed numerical simulations of the two-dimensional time-dependent Schrödinger equation in the laboratory frame using a single-active electron approximation (methodology as in Ref. [26]) on a set of N-fold rotationally symmetric model molecules. They are described by the potential

TABLE II. Predicted leading-order signals in the laboratory frame both in general and for two particular setups analyzed in Ref. [24]. For easier comparison we report the positions in the latter case in terms of the frequency ω of the RCP driver, cf. Eq. (1). The two side-line branches, indicated by I (II) in the table header, correspond to absorption (emission) from the virtual driver, cf. the $\pm$ sign in Table I. Note the opposite convention for RCP and LCP compared to Ref. [24].

		Main	1st side (I)	1st side (II)	2nd side (I)	2nd side (II)
General case, odd N	RCP	$m\tilde{\omega} - \alpha$	$\bar{m}\,\tilde{\omega} + (N-1)\alpha$	$\bar{m}\,\tilde{\omega} - (N+1)\alpha$	$m\tilde{\omega} + (2N-1)\alpha$	$m\tilde{\omega} - (2N+1)\alpha$
($m \in \mathbb{N}$ odd, $\bar{m} \in \mathbb{N}$ even)	LCP	$m\tilde{\omega} + \alpha$	$\bar{m}\,\tilde{\omega} + (N+1)\alpha$	$\bar{m}\,\tilde{\omega} - (N-1)\alpha$	$m\tilde{\omega} + (2N+1)\alpha$	$m\tilde{\omega} - (2N-1)\alpha$
General case, even N	RCP	$m\tilde{\omega} - \alpha$	$m\tilde{\omega} + (N-1)\alpha$	$m\tilde{\omega} - (N+1)\alpha$	$m\tilde{\omega} + (2N-1)\alpha$	$m\tilde{\omega} - (2N+1)\alpha$
($m \in \mathbb{N}$ odd)	LCP	$m\tilde{\omega} + \alpha$	$m\tilde{\omega} + (N+1)\alpha$	$m\tilde{\omega} - (N-1)\alpha$	$m\tilde{\omega} + (2N+1)\alpha$	$m\tilde{\omega} - (2N-1)\alpha$
$N = 3$, $\tilde{\omega} = \frac{3}{2}\omega$, $\alpha = \frac{1}{3}\tilde{\omega} = \frac{1}{2}\omega$	RCP	$3n\omega + \omega$	$3n\omega + \omega$	$3n\omega + \omega$	$3n\omega + \omega$	$3n\omega + \omega$
($n \in \mathbb{N}$)	LCP	$3n\omega + 2\omega$	$3n\omega + 2\omega$	$3n\omega + 2\omega$	$3n\omega + 2\omega$	$3n\omega + 2\omega$
$N = 3$, $\tilde{\omega} = 2\omega$, $\alpha = \frac{1}{2}\tilde{\omega} = \omega$	RCP	$4n\omega + \omega$	$4n\omega + 2\omega$	$4n\omega$	$4n\omega + 3\omega$	$4n\omega + 3\omega$
($n \in \mathbb{N}$)	LCP	$4n\omega + 3\omega$	$4n\omega$	$4n\omega + 2\omega$	$4n\omega + \omega$	$4n\omega + \omega$

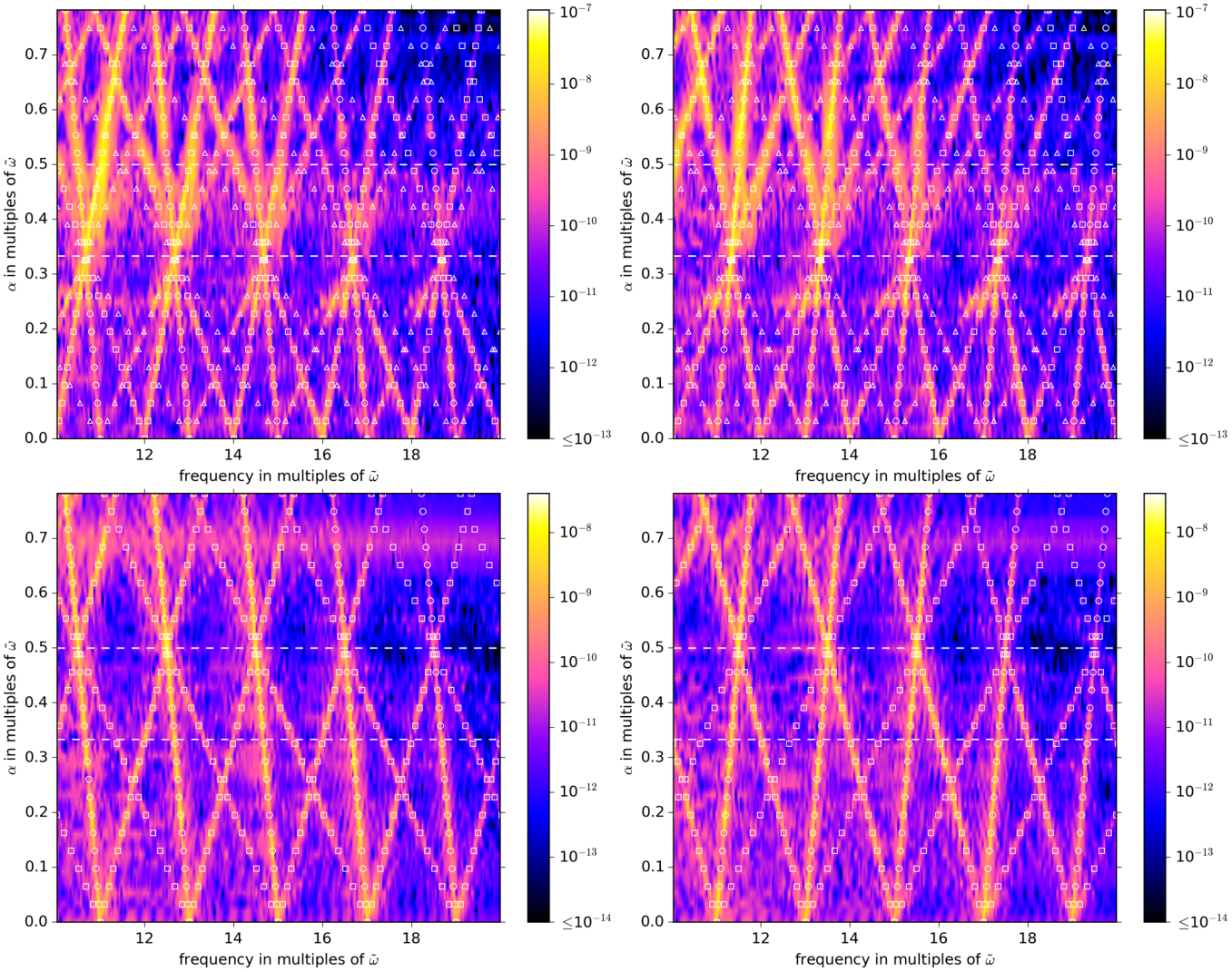

FIG. 2. HHG signal intensity obtained by numerical simulations for $N = 3$ (top) and $N = 4$ (bottom) (left for RCP signal and right for LCP signal). The circles indicate the expected position of the main line; the squares (triangles) indicate the primary (secondary) side line. For reference, two dashed horizontal lines indicate the driving field configurations $\omega' = 2\omega$ (bottom line) and $\omega' = 3\omega$ (top line) in the laboratory frame.

$$V(x,y) = \sum_{p=0}^{N-1} \frac{-Q/N}{\sqrt{[x - R\cos(\frac{2\pi p}{N})]^2 + [y - R\sin(\frac{2\pi p}{N})]^2 + a}},$$

which represents a set of N atomic cores at a distance R from the origin evenly distributed at polar angles $(2\pi p/N)$. We employ a smoothening parameter a for all cores and smear out a total charge Q homogeneously among them (parameter values are given in the Supplemental Material [30]). This model potential represents the simplest form of an N-fold rotational symmetry found in, e.g., diatomic homonuclear molecules ($N = 2$) or the trihydrogen cation H_3^+ ($N = 3$). Moreover, although the specific form of $V_k(x)$ in Eq. (6) depends on the details of the molecular potential, only the underlying N-fold rotational symmetry governs the presence or absence of the characteristic spectral line structure. Consequently, our numerical results are representative even for more complicated molecules like, e.g., benzene C_6H_6 ($N = 6$).

Figure 2 shows the HHG spectra obtained via the expectation value of the dipole acceleration in the laboratory frame of RCP and LCP emission for the threefold and fourfold cases. The strong difference between odd and even N immediately becomes apparent with the primary side lines originating at $\alpha = 0$ for even multiples of $\tilde{\omega}$ when N is odd, cf. the top panels of Fig. 2. Conversely, for even N all main and side lines originate at odd multiples of $\tilde{\omega}$, cf. the bottom panels in Fig. 2. Generally speaking, the primary side lines serve as the fundamental fingerprint of the N-fold rotational symmetry: while the position of the main lines is independent of N, the slope of the primary side lines is directly related to N, cf. Table II. Although the fingerprint of secondary and higher-order side lines is also characteristic for the underlying rotational symmetry their

signal strength is suppressed since these lines originate from high-order contributions from the perturbative virtual driving [larger $|k|$ in Eq. (6)].

Our analysis encompasses the cases of continuous symmetry, i.e., an axially symmetric target, as well as that of no symmetry. Continuous symmetry is formally equivalent to $N \to \infty$ and we therefore predict only the main line to be present in the HHG α scans since the slope of the side lines becomes zero. This is consistent with the results of Ref. [26] where an axially symmetric atomic target was considered. In the absence of symmetry we expect that $N = 1$, i.e., the potential only recurs after a full revolution in the rotating frame. In the Supplemental Material [30] we show that main and side lines according to Table II with $N = 1$ indeed signal the occurrence of symmetry breaking.

In conclusion, we have developed a model for bicircular HHG in the presence of rotational molecular symmetry that explains all principal characteristics of the observed high-order-harmonic emission. Our numerical simulations show that the resulting spectral fingerprint is a reliable indicator of the presence or absence of symmetry for arbitrary driving frequencies. These findings enable the extraction of constructive tomographic information from HHG spectra regarding molecular symmetries and can be employed to track symmetry forming and breaking on ultrafast time scales.

This work was supported by the European Research Council StG (Project No. 277767-TDMET) and the VKR center of excellence QUSCOPE. The numerical results presented in this work were obtained at the Center for Scientific Computing, Aarhus. D. M. R. gratefully acknowledges support from the Alexander von Humboldt Foundation through the Feodor Lynen Program.

[1] T. Popmintchev, M.-C. Chen, P. Arpin, M. M. Murnane, and H. C. Kapteyn, The attosecond nonlinear optics of bright coherent x-ray generation, Nat. Photonics **4**, 822 (2010).

[2] F. Calegari, D. Ayuso, A. Trabattoni, L. Belshaw, S. De Camillis, S. Anumula, F. Frassetto, L. Poletto, A. Palacios, P. Decleva, J. B. Greenwood, F. Martín, and M. Nisoli, Ultrafast electron dynamics in phenylalanine initiated by attosecond pulses, Science **346**, 336 (2014).

[3] P. M. Kraus, B. Mignolet, D. Baykusheva, A. Rupenyan, L. Horný, E. F. Penka, G. Grassi, O. I. Tolstikhin, J. Schneider, F. Jensen, L. B. Madsen, A. D. Bandrauk, F. Remacle, and H. J. Wörner, Measurement and laser control of attosecond charge migration in ionized iodoacetylene, Science **350**, 790 (2015).

[4] T. T. Luu, M. Garg, S. Yu. Kruchinin, A. Moulet, M. Th. Hassan, and E. Goulielmakis, Extreme ultraviolet high-harmonic spectroscopy of solids, Nature (London) **521**, 498 (2015).

[5] A. Rundquist, C. G. Durfee, Z. Chang, C. Herne, S. Backus, M. M. Murnane, and H. C. Kapteyn, Phase-matched generation of coherent soft x-rays, Science **280**, 1412 (1998).

[6] N. Böwering, T. Lischke, B. Schmidtke, N. Müller, T. Khalil, and U. Heinzmann, Asymmetry in Photoelectron Emission from Chiral Molecules Induced by Circularly Polarized Light, Phys. Rev. Lett. **86**, 1187 (2001).

[7] Y. Liu, G. Bian, T. Miller, and T.-C. Chiang, Visualizing Electronic Chirality and Berry Phases in Graphene Systems Using Photoemission with Circularly Polarized Light, Phys. Rev. Lett. **107**, 166803 (2011).

[8] S.-Y. Xu *et al.*, Hedgehog spin texture and Berry's phase tuning in a magnetic topological insulator, Nat. Phys. **8**, 616 (2012).

[9] A. Fleischer, O. Kfir, T. Diskin, P. Sidorenko, and O. Cohen, Spin angular momentum and tunable polarization in high-harmonic generation, Nat. Photonics **8**, 543 (2014).

[10] O. Kfir, P. Grychtol, E. Turgut, R. Knut, D. Zusin, D. Popmintchev, T. Popmintchev, H. Nembach, J. M. Shaw, A. Fleischer, H. Kapteyn, M. Murnane, and O. Cohen, Generation of bright phase-matched circularly-polarized extreme ultraviolet high harmonics, Nat. Photonics **9**, 99 (2015).

[11] O. Kfir, P. Grychtol, E. Turgut, R. Knut, D. Zusin, A. Fleischer, E. Bordo, T. Fan, D. Popmintchev, T. Popmintchev, H. Kapteyn, M. Murnane, and O. Cohen, Helicity-selective phase-matching and quasi-phase matching of circularly polarized high-order harmonics: towards chiral attosecond pulses, J. Phys. B **49**, 123501 (2016).

[12] D. D. Hickstein, F. J. Dollar, P. Grychtol, J. L. Ellis, R. Knut, C. Hernández-García, D. Zusin, C. Gentry, J. M. Shaw, T. Fan, K. M. Dorney, A. Becker, A. Jaroń-Becker, H. C. Kapteyn, M. M. Murnane, and C. G. Durfee, Non-collinear generation of angularly isolated circularly polarized high harmonics, Nat. Photonics **9**, 743 (2015).

[13] T. Fan *et al.*, Bright circularly polarized soft x-ray high harmonics for x-ray magnetic circular dichroism, Proc. Natl. Acad. Sci. U.S.A. **112**, 14206 (2015).

[14] C. Chen, Z. Tao, C. Hernández-García, P. Matyba, A. Carr, R. Knut, O. Kfir, D. Zusin, C. Gentry, P. Grychtol, O. Cohen, L. Plaja, A. Becker, A. Jaron-Becker, H. Kapteyn, and M. Murnane, Tomographic reconstruction of circularly polarized high-harmonic fields: 3d attosecond metrology, Sci. Adv. **2**, e1501333 (2016).

[15] H. Eichmann, A. Egbert, S. Nolte, C. Momma, B. Wellegehausen, W. Becker, S. Long, and J. K. McIver, Polarization-dependent high-order two-color mixing, Phys. Rev. A **51**, R3414 (1995).

[16] S. Long, W. Becker, and J. K. McIver, Model calculations of polarization-dependent two-color high-harmonic generation, Phys. Rev. A **52**, 2262 (1995).

[17] R. Zerne, C. Altucci, M. Bellini, M. B. Gaarde, T. W. Hänsch, A. L'Huillier, C. Lyngå, and C.-G. Wahlström, Phase-Locked High-Order Harmonic Sources, Phys. Rev. Lett. **79**, 1006 (1997).

[18] W. Becker, B. N. Chichkov, and B. Wellegehausen, Schemes for the generation of circularly polarized high-order harmonics by two-color mixing, Phys. Rev. A **60**, 1721 (1999).

[19] D. B. Milošević, W. Becker, and R. Kopold, Generation of circularly polarized high-order harmonics by two-color coplanar field mixing, Phys. Rev. A **61**, 063403 (2000).

[20] D. B. Milošević and W. Becker, Attosecond pulse trains with unusual nonlinear polarization, Phys. Rev. A **62**, 011403 (2000).

[21] E. Pisanty, S. Sukiasyan, and M. Ivanov, Spin conservation in high-order-harmonic generation using bicircular fields, Phys. Rev. A **90**, 043829 (2014).

[22] D. B. Milošević, High-order harmonic generation by a bichromatic elliptically polarized field: conservation of angular momentum, J. Phys. B **48**, 171001 (2015).

[23] L. Medišauskas, J. Wragg, H. van der Hart, and M. Yu. Ivanov, Generating Isolated Elliptically Polarized Attosecond Pulses Using Bichromatic Counterrotating Circularly Polarized Laser Fields, Phys. Rev. Lett. **115**, 153001 (2015).

[24] F. Mauger, A. D. Bandrauk, and T. Uzer, Circularly polarized molecular high harmonic generation using a bicircular laser, J. Phys. B **49**, 10LT01 (2016).

[25] D. Baykusheva, M. S. Ahsan, N. Lin, and H. J. Wörner, Bicircular High-Harmonic Spectroscopy Reveals Dynamical Symmetries of Atoms and Molecules, Phys. Rev. Lett. **116**, 123001 (2016).

[26] D. M. Reich and L. B. Madsen, Rotating-frame perspective on high-order-harmonic generation of circularly polarized light, Phys. Rev. A **93**, 043411 (2016).

[27] V. Averbukh, O. E. Alon, and N. Moiseyev, Crossed-beam experiment: High-order harmonic generation and dynamical symmetry, Phys. Rev. A **60**, 2585 (1999).

[28] F. Ceccherini, D. Bauer, and F. Cornolti, Dynamical symmetries and harmonic generation, J. Phys. B **34**, 5017 (2001).

[29] F. Ceccherini and D. Bauer, Harmonic generation in ring-shaped molecules, Phys. Rev. A **64**, 033423 (2001).

[30] See Supplemental Material at http://link.aps.org/supplemental/10.1103/PhysRevLett.117.133902, which generalizes our model to the many-electron case and provides further evidence for its predictive power by showing numerical results for HHG signals for even more N-fold rotational symmetries as well as in the absence of rotational symmetry.

[31] P. B. Corkum, Plasma Perspective on Strong Field Multiphoton ionization, Phys. Rev. Lett. **71**, 1994 (1993).

[32] K. J. Schafer, B. Yang, L. F. DiMauro, and K. C. Kulander, Above Threshold Ionization Beyond the High Harmonic Cutoff, Phys. Rev. Lett. **70**, 1599 (1993).

[33] M. Lewenstein, P. Balcou, M. Yu. Ivanov, A. L'Huillier, and P. B. Corkum, Theory of high-harmonic generation by low-frequency laser fields, Phys. Rev. A **49**, 2117 (1994).